NASA/TM—2014-218329

Computational Simulations of Convergent Nozzles for the AIAA 1st Propulsion Aerodynamics Workshop

Vance F. Dippold, III
Glenn Research Center, Cleveland, Ohio

August 2014

NASA STI Program . . . in Profile

Since its founding, NASA has been dedicated to the advancement of aeronautics and space science. The NASA Scientific and Technical Information (STI) program plays a key part in helping NASA maintain this important role.

The NASA STI Program operates under the auspices of the Agency Chief Information Officer. It collects, organizes, provides for archiving, and disseminates NASA's STI. The NASA STI program provides access to the NASA Aeronautics and Space Database and its public interface, the NASA Technical Reports Server, thus providing one of the largest collections of aeronautical and space science STI in the world. Results are published in both non-NASA channels and by NASA in the NASA STI Report Series, which includes the following report types:

- TECHNICAL PUBLICATION. Reports of completed research or a major significant phase of research that present the results of NASA programs and include extensive data or theoretical analysis. Includes compilations of significant scientific and technical data and information deemed to be of continuing reference value. NASA counterpart of peer-reviewed formal professional papers but has less stringent limitations on manuscript length and extent of graphic presentations.

- TECHNICAL MEMORANDUM. Scientific and technical findings that are preliminary or of specialized interest, e.g., quick release reports, working papers, and bibliographies that contain minimal annotation. Does not contain extensive analysis.

- CONTRACTOR REPORT. Scientific and technical findings by NASA-sponsored contractors and grantees.

- CONFERENCE PUBLICATION. Collected papers from scientific and technical conferences, symposia, seminars, or other meetings sponsored or cosponsored by NASA.

- SPECIAL PUBLICATION. Scientific, technical, or historical information from NASA programs, projects, and missions, often concerned with subjects having substantial public interest.

- TECHNICAL TRANSLATION. English-language translations of foreign scientific and technical material pertinent to NASA's mission.

Specialized services also include creating custom thesauri, building customized databases, organizing and publishing research results.

For more information about the NASA STI program, see the following:

- Access the NASA STI program home page at *http://www.sti.nasa.gov*

- E-mail your question to *help@sti.nasa.gov*

- Fax your question to the NASA STI Information Desk at 443–757–5803

- Phone the NASA STI Information Desk at 443–757–5802

- Write to:
  STI Information Desk
  NASA Center for AeroSpace Information
  7115 Standard Drive
  Hanover, MD 21076–1320

NASA/TM—2014-218329

Computational Simulations of Convergent Nozzles for the AIAA 1st Propulsion Aerodynamics Workshop

Vance F. Dippold, III
Glenn Research Center, Cleveland, Ohio

National Aeronautics and
Space Administration

Glenn Research Center
Cleveland, Ohio 44135

August 2014

Acknowledgments

This work was supported by the Fundamental Aeronautics Program's Subsonic Fixed-Wing and High Speed Projects.

This work was sponsored by the Fundamental Aeronautics Program at the NASA Glenn Research Center.

Level of Review: This material has been technically reviewed by technical management.

Available from

NASA Center for Aerospace Information
7115 Standard Drive
Hanover, MD 21076–1320

National Technical Information Service
5301 Shawnee Road
Alexandria, VA 22312

Available electronically at http://www.sti.nasa.gov

Computational Simulations of Convergent Nozzles for the AIAA 1st Propulsion Aerodynamics Workshop

Vance F. Dippold, III
National Aeronautics and Space Administration
Glenn Research Center
Cleveland, Ohio 44135

Abstract

Computational Fluid Dynamics (CFD) simulations were completed for a series of convergent nozzles in participation of the American Institute of Aeronautics and Astronautics (AIAA) 1st Propulsion Aerodynamics Workshop. The simulations were performed using the Wind-US flow solver. Discharge and thrust coefficients were computed for four axisymmetric nozzles with nozzle pressure ratios (NPR) ranging from 1.4 to 7.0. The computed discharge coefficients showed excellent agreement with available experimental data; the computed thrust coefficients captured trends observed in the experimental data, but over-predicted the thrust coefficient by 0.25 to 1.0 percent. Sonic lines were computed for cases with NPR ≥ 2.0 and agreed well with experimental data for NPR ≥ 2.5. Simulations were also performed for a 25° conic nozzle bifurcated by a flat plate at NPR = 4.0. The jet plume shock structure was compared with and without the splitter plate to the experimental data. The Wind-US simulations predicted the shock structure well, though lack of grid resolution in the plume reduced the sharpness of the shock waves. Unsteady Reynolds-Averaged Navier-Stokes (URANS) simulations and Detached Eddy Simulations (DES) were performed at NPR = 1.6 for the 25° conic nozzle with splitter plate. The simulations predicted vortex shedding from the trailing edge of the splitter plate. However, the vortices of URANS and DES solutions appeared to dissipate earlier than observed experimentally. It is believed that a lack of grid resolution in the region of the vortex shedding may have caused the vortices to break down too soon.

Nomenclature

A	area
C_d	nozzle discharge coefficient
C_V	nozzle thrust coefficient, integrated across jet only
$C_{V,\text{total}}$	total nozzle thrust coefficient, integrated across jet and base region
D	diameter
M	Mach number
NPR	nozzle pressure ratio
p	pressure
R	gas constant; 1716 (ft×lb)/(slug×°R)
r	radius
T	temperature
u	velocity in streamwise (x-) direction
x,y,z	orthogonal coordinate system
y^+	non-dimensional wall distance
γ	ratio of specific heats; 1.4
ρ	density

Subscripts:

0	total condition
jet	jet condition
nozzle	full nozzle, jet and base area
wall	wall condition
∞	freestream static condition

Introduction

In 2012, the Air-Breathing Propulsion Technical Committees of the American Institute of Aeronautics and Astronautics (AIAA) conducted the 1st Propulsion Aerodynamics Workshop. The objectives of the 1st Propulsion Aerodynamics Workshop were as follows:

1. To assess the accuracy of computational fluid dynamics for air breathing propulsion applications;
2. To assess current numerical prediction capability;
3. To develop practical guidelines for 2-D and 3-D simulations.

Workshop participants from government, academia, and industry completed Computational Fluid Dynamics (CFD) simulations of problems relevant to air-breathing propulsion: an S-duct and a series of convergent nozzles. Each participant presented their results at the workshop, held prior to the 48th Joint Propulsion Conference, in Atlanta in July 2012. Some of the CFD studies were performed as blind trials and compared with the available experimental data during the workshop. After each participant had presented their results, the workshop committee compared the results from all of the participants and compared their results with experimental data. The workshop committee presented follow-up reports for the nozzle cases (Ref. 1) and the S-duct cases (Ref. 2) at the 49th Joint Propulsion Conference, held in San Jose in July 2013. Several participants also published reports with their findings (Ref. 3). This paper discusses computational simulations performed for the series of convergent nozzles as a part of the 1st Propulsion Aerodynamics Workshop.

CFD simulations were performed for a series of four single-stream, axisymmetric, convergent nozzles at nozzle pressure ratios (NPR)—the ratio of nozzle total pressure to ambient static pressure—ranging from 1.4 to 7.0. The nozzle geometries consisted of a reference nozzle, with a circular-arc wall contour, and three conical nozzles, with half angles of 15°, 25°, and 40°. The internal nozzle geometries are illustrated in Figure 1. Each nozzle had an exit diameter of 3.0 in. Experimental data was collected for these nozzles by Thornock and Brown (Ref. 4). The experimental nozzles consisted of two halves, between which a splitter plate was inserted. The splitter plate included an array of pressure taps that were used to compute local Mach number inside the nozzle. Thornock and Brown reported the discharge and thrust coefficients for each nozzle and NPR combination. Using the splitter plate pressure taps, the sonic line was also determined. Spark shadowgraph images, while not presented in the original report, were compared to CFD solutions at the Propulsion Aerodynamics Workshop for select nozzle and NPR combinations in the follow-up report (Ref. 1). The shadowgraph images showed the plume shock structure for a nozzle at supersonic NPR and unsteady vortex shedding for one nozzle at a subsonic NPR.

The Propulsion Aerodynamics Workshop had three Instances for the nozzle cases. Instance 1 consisted of simulating all four nozzle geometries, without splitter plates, with NPRs ranging from 1.4 to 4.0. The predicted discharge coefficient, thrust coefficient, and sonic line would be compared to experimental data. Instance 2 consisted of simulating the 25° conic nozzle with NPR = 4.0, with and without the splitter plate. The plume flowfield—specifically, the series of shock waves and expansion waves—would be compared to shadowgraph images. Finally, Instance 3 consisted of a time-accurate simulation of the 25° conic nozzle with splitter plate for NPR = 1.6. The simulated vortex shedding from the trailing edge of the splitter plate would be compared to the vortex shedding observed in a spark shadowgraph image.

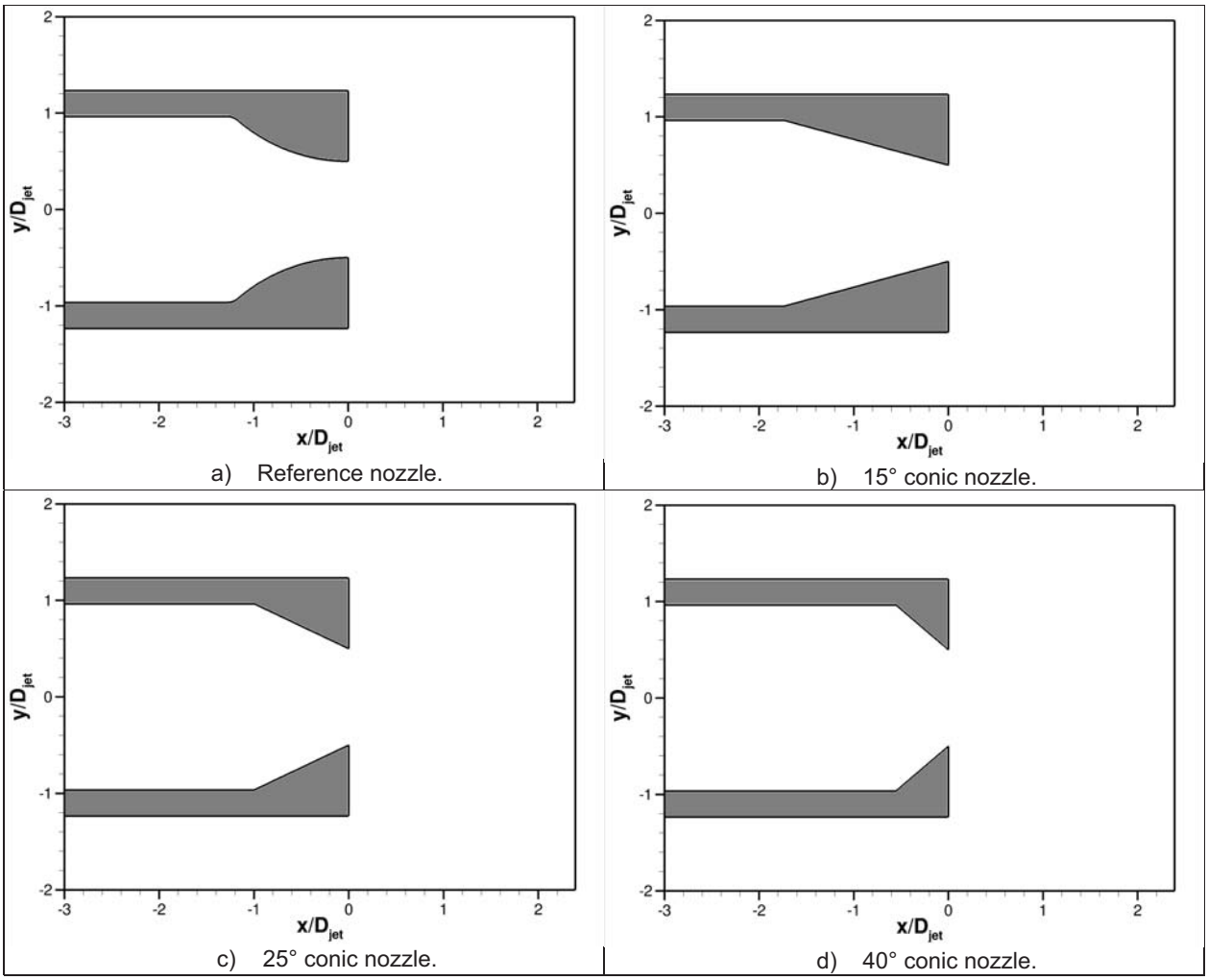

Figure 1.—Flow lines of nozzles.

This series of nozzle simulations tests a broad range of a CFD code's capabilities: the ability to predict mass flow and thrust, the ability to predict and resolve plume shock structures, and the ability to predict and resolve unsteady phenomena. Successfully simulating and predicting these elements is key to using CFD simulations to help design and improve modern aircraft propulsion systems.

Nozzle Cases and Flow Conditions

The 1st Propulsion Aerodynamics Workshop nozzle problem consisted of three Instances, which are described below.

Instance 1

Instance 1 consisted of 40 total CFD simulations of four axisymmetric, convergent nozzles with NPR ranging from 1.4 to 7.0. The four nozzle geometries consisted of a reference nozzle, with a circular-arc wall contour radius of 5.449 in. (Ref. 1), and three conic nozzles, with half angles of 15°, 25°, and 40°. The nozzle exit diameter was 3.0 in. for each nozzle. Each nozzle also had a rather thick base region, giving the nozzle a total diameter of 7.5 in. at the exit plane. The axisymmetric nozzle geometries are shown in Figure 1. Table 1 shows the distinct NPRs for which each nozzle was simulated. The discharge

TABLE 1.—INSTANCE 1 NOZZLES AND NOZZLE PRESSURE RATIOS

Nozzle	Nozzle Pressure Ratio (NPR)										
	1.4	1.6	1.8	2.0	2.5	3.0	3.5	4.0	5.0	6.0	7.0
Reference	X	---	X	X	---	X	---	X	X	X	X
15° Conic	X	X	X	X	X	X	---	X	X	X	X
25° Conic	X	X	X	X	X	X	X	X	X	X	X
40° Conic	X	X	X	X	X	X	X	X	X	X	X

coefficient and thrust coefficient from all simulations were reported for the Propulsion Aerodynamics Workshop and were compared with experimental data. Additionally, the static pressure was sampled at specific locations along the interior surface of the nozzle and through the jet plume that corresponded to pressure taps along the nozzle wall and splitter plate in the experiment. The wall equivalent Mach number was calculated using these local static pressures. The wall equivalent Mach number was reported to the Propulsion Aerodynamics Workshop and used to compute the sonic line for each jet. The sonic line data were compared to experimental data. The details of the discharge coefficient, thrust coefficient, and sonic line calculations will be more fully discussed in the Results section.

Instance 2

Instance 2 involved comparing the plume shock structure of the 25° conic nozzle with and without the splitter plate for a NPR of 4.0. The axisymmetric solution of the 25° conic nozzle without the splitter plate from Instance 1 was used. Therefore, only a 3-D simulation of the 25° conic nozzle with splitter plate was run for Instance 2. The splitter plate was 0.0625 in. thick and extended 12.6 in. upstream into the nozzle and 3.0 in. downstream of the nozzle. The splitter plate was 7.5 in. wide—the width of the entire nozzle, including the base region. The experimental splitter plate contained an array of 128 static pressure taps, which were used to calculate Mach number and the sonic line. The addition of the splitter plate increased the diameter of the nozzle to 3.0625 in. along the axis perpendicular to the plate. The location of the first shock wave downstream of the nozzle was compared between the two solutions. Additionally, the CFD solutions were compared with experimentally-obtained spark shadowgraph images for their respective case.

Instance 3

The goal of Instance 3 was to test the CFD solver's ability to predict vortex shedding from the trailing end of the splitter plate for the 25° conic nozzle with splitter plate with a NPR of 1.6. The vortex shedding was a surprising phenomenon that was observed experimentally and recorded in a spark shadowgraph image (Ref. 1). A time-accurate simulation was needed to obtain the vortex shedding.

Numerical Methods

Wind-US Flow Solver

Wind-US, version 2.0 (Refs. 5 and 6), was used to run the computational fluid dynamics (CFD) simulations of the convergent nozzles. The Wind-US code is a general-purpose, Reynolds-Averaged Navier-Stokes (RANS) CFD solver for both structured and unstructured grids. The code is developed and managed by the NPARC Alliance, a partnership between NASA GRC, USAF Arnold Engineering Development Complex, and The Boeing Company. The Wind-US code offers several numerical schemes, as well as several zero-, one-, and two-equation turbulence models. The Wind-US code includes the second-order Roe numerical scheme and the Menter Shear Stress Transport (SST) turbulence model (Ref. 7), both of which were used for these simulations.

For all simulations, the jet exhausted the nozzle into a quiescent freestream, with a static temperature of 500 °R, and static pressure of 14.7 psi. While the freestream was quiescent, the freestream Mach number was 0.01. It has been found that compressible flow solvers, like Wind-US, struggle with convergent nozzle flows when the freestream velocity is set to zeroeven a small freestream velocity helps the solver converge the solution more quickly. At the nozzle inflow, the total temperature was set to 500 °R; the total pressure was set according to the NPR (see Table 1) and the freestream static pressure:

$$p_0 = \mathrm{NPR} \cdot p_\infty \tag{1}$$

The downstream outflow was set to the freestream static pressure, 14.7 psi.

Grid Strategy

A total of five structured, point-matched grids were constructed with the commercially-available Pointwise (Pointwise, Inc.) grid generation software: four axisymmetric grids for the reference nozzle and three conic nozzles; one 3-D grid for the 25° conic nozzle with splitter plate. Grids for the four axisymmetric nozzles are shown in Figure 2. Inside the nozzle, the grids had between 161 and 193 grid points in the streamwise direction and 65 grid points in the radial direction, between the centerline and the interior wall of the nozzle. Beyond the nozzle exit, the grids continued for 50 jet diameters downstream of

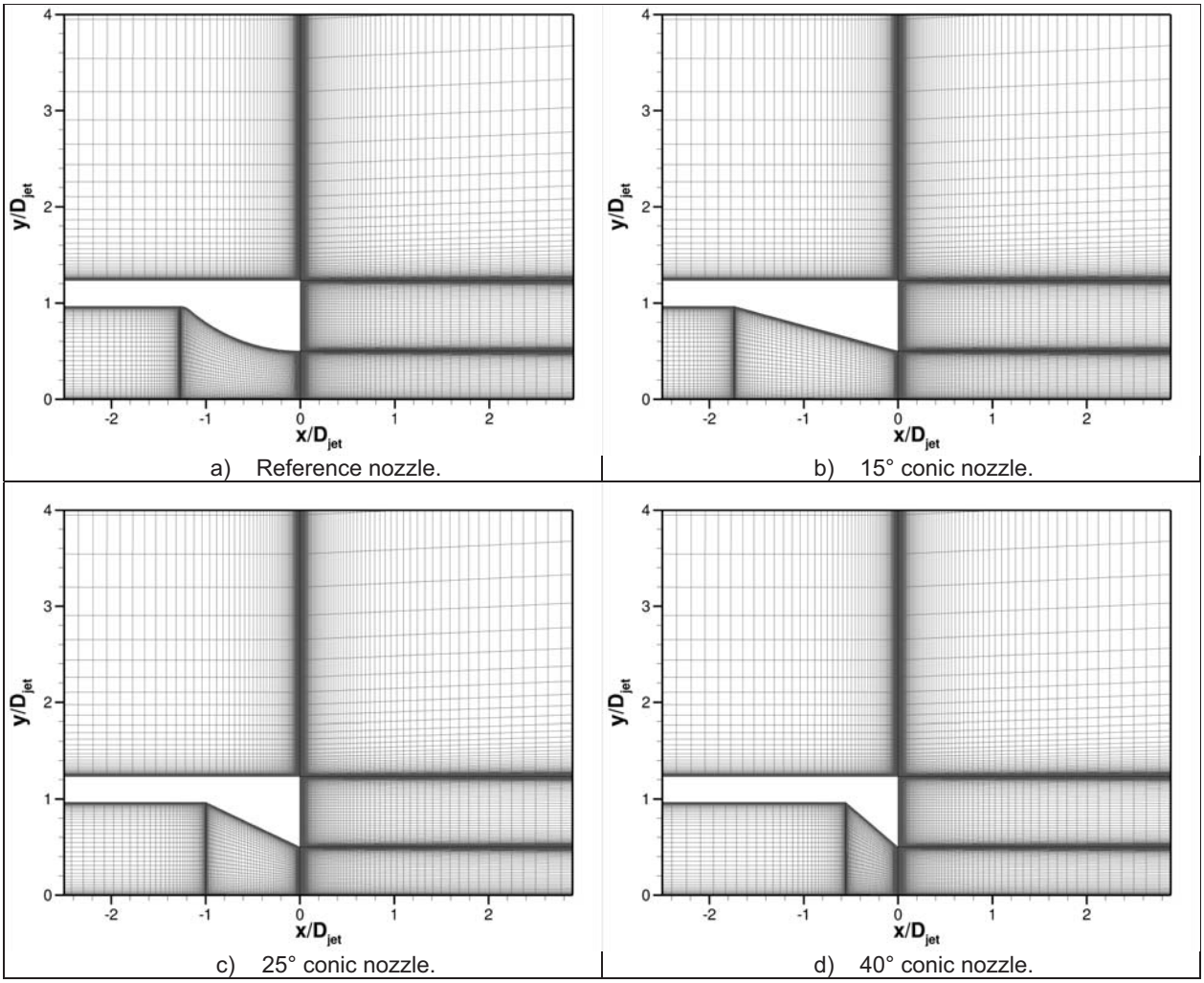

Figure 2.—Grids for axisymmetric nozzles.

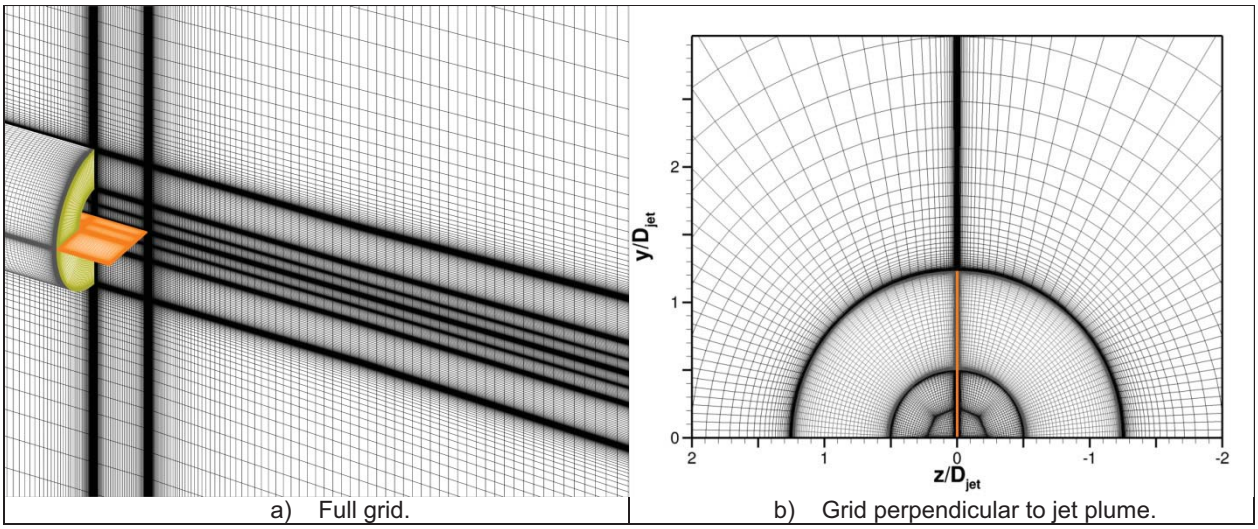

a) Full grid. b) Grid perpendicular to jet plume.

Figure 3.—Grid for 25° conic nozzle with splitter plate.

the nozzle exit, containing 221 grid points. The grids extended 23 jet diameters radially outward of the nozzle, containing 233 grid points. The axisymmetric reference nozzle grid consisted of 74,000 grid points. Each axisymmetric conic nozzle consisted of 71,000 grid points. In order to properly resolve the boundary layers along the viscous walls inside the nozzle, grid points were clustered at the walls, with an initial grid point spacing of 1.0e-4 in., resulting in a nominal y^+ value of 2. It has been shown that the non-dimensional wall spacing, y^+, of the first grid point off the wall needs to be on the order of 1.0 (Refs. 8 and 9) for RANS solvers to adequately resolve the boundary layer. The axisymmetric grids were composed of 6 zones.

The 3-D grid for the 25° conic nozzle with splitter plate is shown in Figure 3. The grid took advantage of symmetry: only a 180° sector was modeled, with the symmetry plane being perpendicular to the splitter plate. The 3-D grid was constructed in a manner similar to the axisymmetric 25° conic nozzle. Figure 3(b) shows the grid perpendicular to the jet plume at the trailing edge of the splitter plate. Grid points were also clustered radially towards the splitter plate (1.0e-4 in.) and clustered axially at the splitter plate trailing edge (1.0e-4 in.). There were 121 points along the splitter plate in the streamwise direction. The 3-D grid for the 25° conic nozzle with splitter plate consisted of 14 million grid points. The grid was split into 68 zones to improve performance on multi-processor computer systems.

Convergence

To speed up convergence of each solution, each simulation was solved by sequencing through three grid resolutions: first, the solution was solved using every fourth grid point, then using every second grid point, and finally using every grid point. Solving on the coarser grids first allowed the overall flowfield to set up rather quickly before solving the turbulence details in the finest grid. This grid sequencing approach is standard practice for structured RANS calculations. Furthermore, converging the solution on multiple grid sequence levels helped ensure that the finest grid solution was not dependent on the grid (i.e., the solution would not change significantly if minor changes to the grid were made). For all cases, discharge coefficient and thrust coefficient were monitored for convergence. Additionally, the streamwise velocity and the turbulent kinetic energy along the nozzle centerline were monitored for Instance 1 and Instance 2. The solutions were considered converged when the discharge and thrust coefficients varied by less than 0.01 percent over 10,000 iterations and the centerline velocity and turbulent kinetic energy varied by less than 0.1 percent over 10,000 iterations.

Due to the large number of cases that had to be completed for the workshop, a "set it and forget it" approach was applied to the steady-state solutions in Instance 1 and Instance 2: the final Courant-Freidrichs-Levy (CFL) number was set to 0.10 to ensure stability; each solution was run for 70,000 to 120,000 iterations to ensure convergence. For cases with NPR ≤ 2.0, the jet plumes exhibited behavior that seemed reminiscent of unsteady behavior: the velocity and turbulent kinetic energy along the centerline fluctuated and were not converging. Similar behavior has been observed before, for simulations of high-subsonic and transonic flows through convergent nozzles. The procedure to obtain a converged solution was to run these simulations with constant time-steps. Time-steps of 1.0e-8 sec were used for a few of the 15° conic nozzle solutions; these cases required up to 800,000 iterations to fully converge. Later constant time-step solutions (including all the 25° and 40° conic nozzles with NPR ≤ 2.0) used time-steps of 2.0e-8 sec and needed 300,000 iterations to converge. For the unsteady solution in Instance 3, two analyses were performed: an unsteady RANS (URANS) simulation and a detached eddy simulation (DES). For both unsteady simulations, a constant time step of 1.0e-8 sec was used. The unsteady simulations were run long enough for the vortex shedding to set up sufficiently, 400,000 to 500,000 iterations. All Wind-US simulations were performed on Linux (Linus Torvalds) computers, primarily the multi-node, multi-core NASA Advanced Supercomputing (NAS) Pleiades supercomputer (Ref. 10).

Results

CFD simulations were performed as previously mentioned. The typical convergence of the discharge coefficient and the thrust coefficient is illustrated in Figure 4. Based on the discharge and thrust coefficients, most solutions were adequately converged by 50,000 iterations. Figure 5 shows the streamwise velocity and turbulent kinetic energy along the centerline for the typical Instance 1 nozzle solution. Again, the solution was adequately converged much earlier than the full run (120,000 iterations), often by 60,000 to 70,000 iterations. Nonetheless, allowing the simulations to run 120,000 iterations guaranteed that most solutions were fully converged. As mentioned previously, the conic nozzles with low NPR 1.4 to 2.0 did exhibit unsteady-like behaviors and required a constant time-step simulation with 300,000 or more iterations to fully converge.

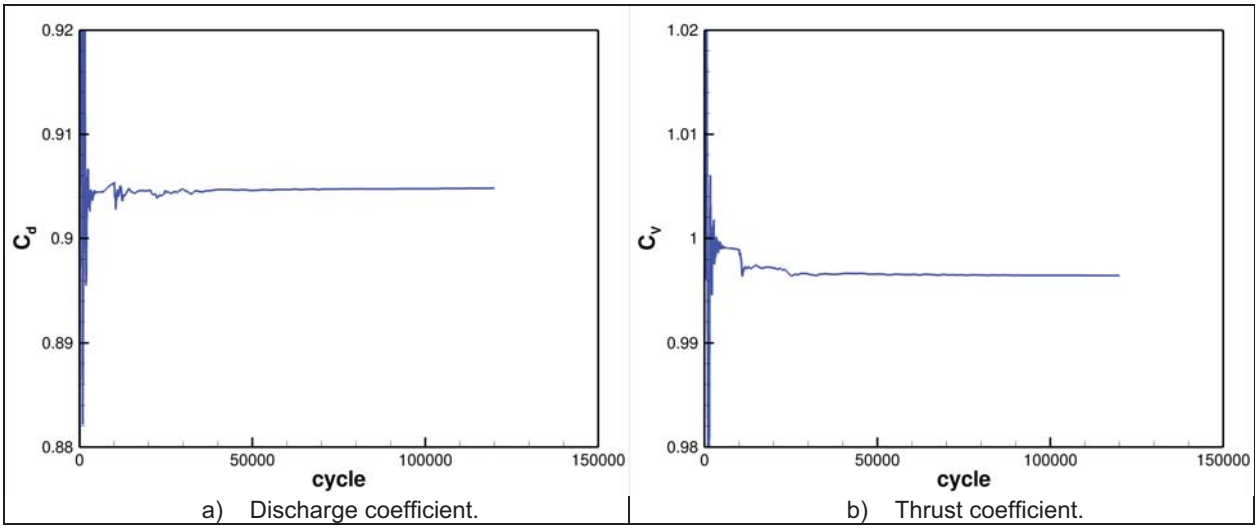

a) Discharge coefficient. b) Thrust coefficient.

Figure 4.—Typical convergence of nozzle discharge and thrust coefficients (shown for 40° conic nozzle with NPR = 4.0).

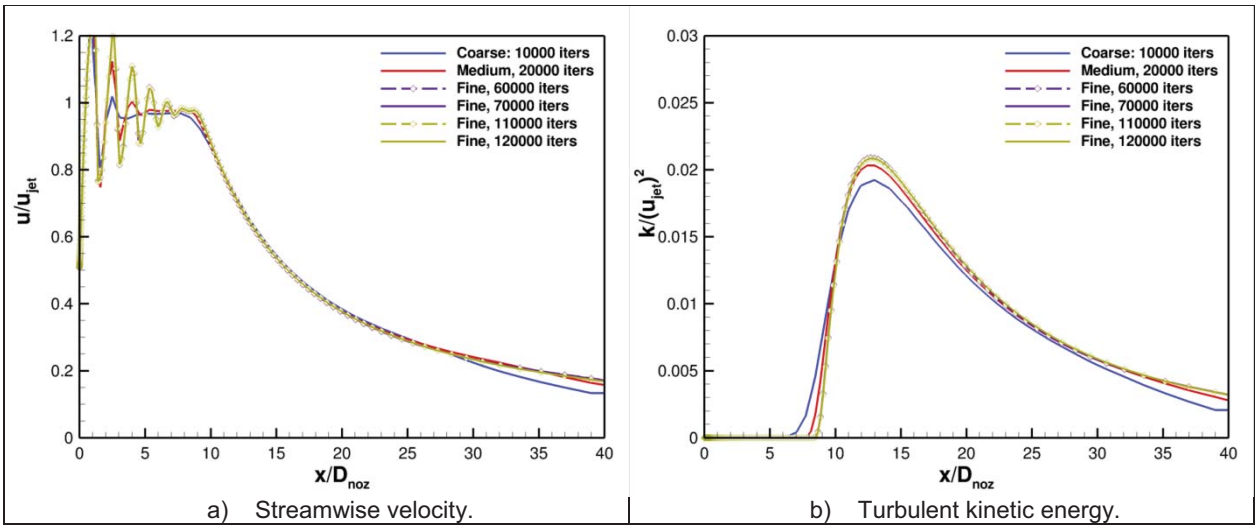

a) Streamwise velocity. b) Turbulent kinetic energy.

Figure 5.—Typical convergence of nozzle centerline streamwise velocity and turbulent kinetic energy (shown for 40° conic nozzle with NPR = 4.0).

Instance 1

A total of 40 axisymmetric nozzle solutions were computed for Instance 1. The nozzle pressure ratios (ranging from 1.4 to 7.0) were applied to four convergent nozzle geometries according to Table 1. The discharge coefficient, C_d, and thrust coefficient, C_V, were computed for each solution as follows:

$$C_d \equiv \frac{2\pi \cdot \int_0^{r_{\text{jet}}} \rho \cdot u \cdot r \cdot dr}{\rho_{\text{jet}} \cdot U_{\text{jet}} \cdot A_{\text{jet}}} \tag{2}$$

$$C_V \equiv \frac{2\pi \cdot \int_0^{r_{\text{jet}}} \left[\rho \cdot u^2 \cdot (p - p_\infty)\right] \cdot r \cdot dr}{U_{\text{jet}} \cdot \int_0^{r_{\text{jet}}} \rho \cdot u \cdot r \cdot dr} \tag{3}$$

The standard discharge coefficient, C_d, and thrust coefficient, C_V, are computed over the radius of the nozzle exit, r_{jet}, using the local density (ρ), local streamwise velocity (u), and local radius from the centerline (r). The resultant nozzle exit area, A_{jet}, was 7.0686 in.^{2}. The ideal jet velocity, U_{jet}, is computed from the Mach number of the ideally expanded jet, M_{jet}, and the temperature of the jet, T_{jet}, all found in the following equations:

$$U_{\text{jet}} = M_{\text{jet}} \cdot \sqrt{\gamma \cdot R \cdot T_{\text{jet}}} \tag{4}$$

$$M_{\text{jet}} = \sqrt{\left(\frac{2}{\gamma - 1}\right) \cdot \left(NPR^{\left(\frac{\gamma-1}{\gamma}\right)} - 1\right)} \tag{5}$$

$$T_{jet} = T_0 \cdot \left[1 + \left(\frac{\gamma - 1}{2}\right) \cdot M_{\text{jet}}^2\right]^{-1} \tag{6}$$

TABLE 2.—IDEAL JET MACH NUMBER AND VELOCITY FOR EACH NOZZLE PRESSURE RATIO

NPR	M_{jet}	U_{jet} [ft/s]
1.4	0.710	742.0
1.6	0.848	868.7
1.8	0.956	963.6
2.0	1.046	1038.8
2.5	1.223	1176.2
3.0	1.358	1272.0
3.5	1.467	1344.3
6.0	1.559	1401.5
5.0	1.709	1487.9
6.0	1.828	1551.3
7.0	1.928	1600.5

The values of M_{jet} and U_{jet} are shown for each NPR in Table 2. The discharge coefficient from each nozzle solution is plotted in Figure 6 along with the experimental data (available for the 15°, 25°, and 40° conic nozzle cases). The Wind-US solution discharge coefficients show excellent agreement with the experimental data. For each nozzle, the discharge coefficient increases with NPR before becoming relatively constant at larger NPRs. The reference nozzle has the largest discharge coefficient (0.995), followed by the 15° conic nozzle (0.969), the 25° conic nozzle (0.946), and the 40° conic nozzle (0.914). The CFD results show that the nozzle is less efficient at passing flow as the nozzle half-angle increases. The thrust coefficient from each nozzle solution is plotted in Figure 7 along with the experimental data. In contrast to the discharge coefficient, the thrust coefficient increases as the nozzle half-angle increases.

Additionally, the thrust coefficient is relatively constant at smaller NPRs, but decreases substantially (4.0 to 5.0 percent) as NPR increases. Finally, the thrust coefficients from Wind-US are generally 0.5 to 1.5 percent larger than the experimental thrust coefficients.

There was concern as to why such a large disparity exists between the CFD and experimental thrust coefficients. It is clear from the definition of the thrust coefficient equation (Eq. (3)), that only the force across the jet exit is considered. However, the nozzles had a large base region—525 percent the size of the actual nozzle exit area—and surely there was a significant force on the base region that could have affected the experimental thrust measurements. Therefore a new total thrust coefficient was computed:

$$C_{V,\text{Total}} \equiv \frac{2\pi \cdot \int_0^{r_{\text{nozzle}}} \left[\rho \cdot u^2 \cdot (p - p_\infty)\right] \cdot r \cdot dr}{U_{jet} \cdot \int_0^{r_{\text{nozzle}}} \rho \cdot u \cdot r \cdot dr} \tag{7}$$

In this definition of total thrust coefficient, r_{nozzle} is the radius to the outer edge of the nozzle exterior, which includes the large base area. The total thrust coefficient is plotted in Figure 8. The Wind-US total thrust coefficients for each nozzle solution are 0.25 to 0.5 percent smaller than the original thrust coefficient in Figure 7. However, there is still a substantial difference between the CFD total thrust coefficients and the experimental thrust coefficients. It is interesting to note that the total thrust coefficient for the 15° conic nozzle is now the largest thrust coefficient for NPR ≤ 4.0; this does agree with the experimental results.

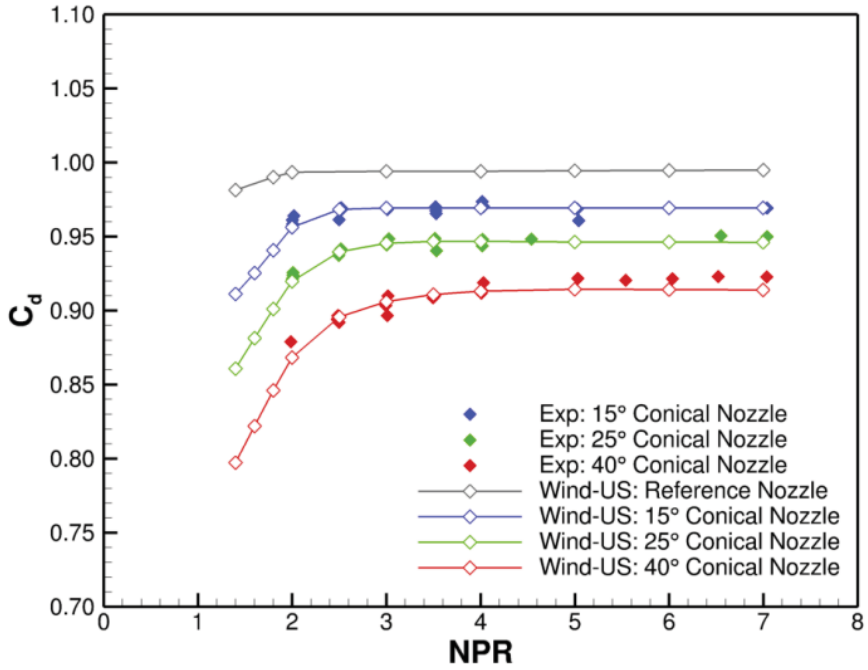

Figure 6.—Discharge coefficient, plotted for all solutions in Instance 1.

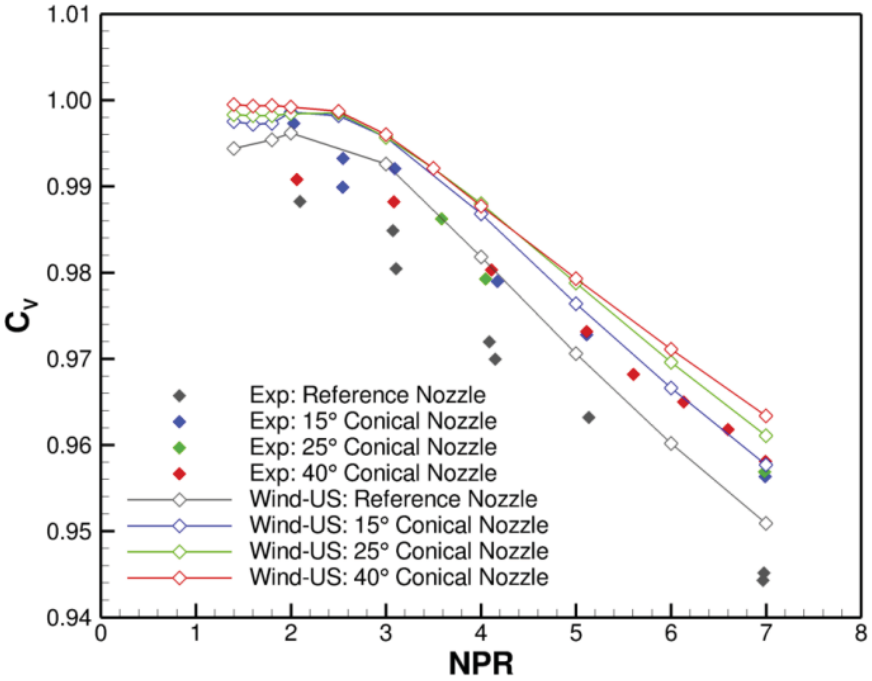

Figure 7.—Thrust coefficient, plotted for all solutions in Instance 1.

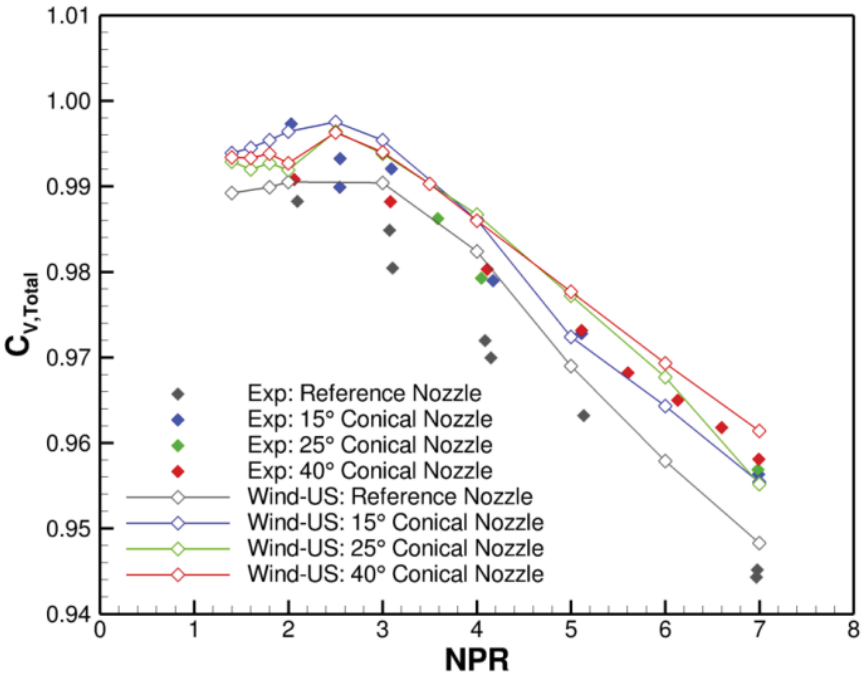

Figure 8.—Total thrust coefficient, plotted for all solutions in Instance 1.

Static pressure data was collected for each nozzle solution at specific points along the nozzle interior wall and at specific points on the nozzle splitter plate. From the wall static pressure, p_{wall}, and the nozzle total pressure (assuming there are no loses), p_0, the wall equivalent Mach number was computed at each specific point:

$$M_{wall} = \sqrt{\left(\frac{2}{\gamma - 1}\right) \cdot \left[\left(\frac{p_0}{p_{wall}}\right)^{\left(\frac{\gamma - 1}{\gamma}\right)} - 1\right]} \tag{8}$$

Interpolation was performed using the wall equivalent Mach number and the location of each static pressure tap to determine the location of the sonic line ($M_{wall} = 1.0$) for the conic nozzle solutions with NPR ≥ 2.0. Sonic lines are plotted in Figure 9 for the conic nozzles with NPR = 2.5. As the half-angle of the nozzle increases, the sonic line is pushed further downstream. The Wind-US solutions show excellent agreement with the experimental data. Figure 10 shows the sonic lines for the 25° conic nozzle for NPR ranging from 2.0 to 5.0. The jet flow becomes supersonic earlier for the larger NPR. The Wind-US solutions show the best agreement with the experimental data for the larger NPR.

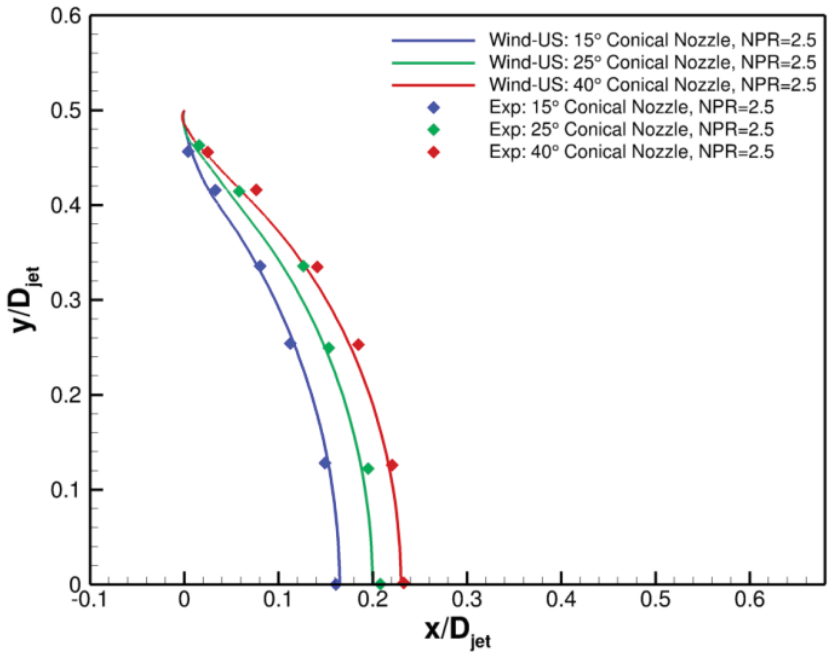

Figure 9.—Comparison of sonic lines for conic nozzles with NPR = 2.5.

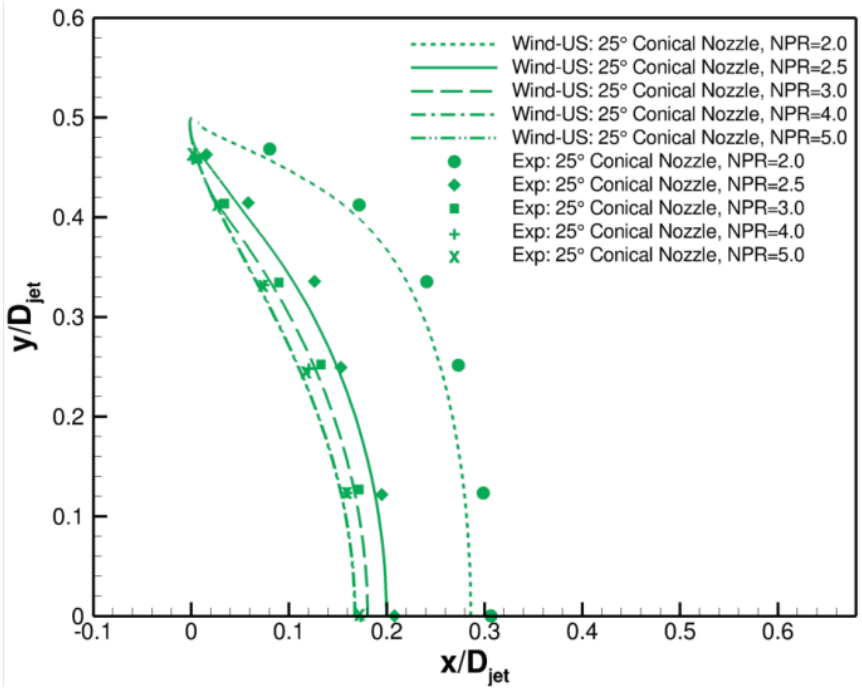

Figure 10.—Comparison of sonic lines for 25° conic nozzle for range of NPRs.

Instance 2

A new 3-D nozzle solution was computed for Instance 2: the 25° conic nozzle with the splitter plate was run with NPR = 4.0. The 3-D solution was compared to the solution of the corresponding axisymmetric, 25° conic nozzle without the splitter plate (obtained in Instance 1). Additionally, both CFD solutions were compared to experimental shadowgraph images. In Figure 11, simulated shadowgraph images of the two nozzle solutions are compared. These simulated shadowgraph images plot the gradient of the density:

$$\nabla\rho = \sqrt{\left(\frac{\partial\rho}{\partial x}\right)^2 + \left(\frac{\partial\rho}{\partial y}\right)^2 + \left(\frac{\partial\rho}{\partial z}\right)^2} \tag{9}$$

The blue line indicates the beginning of the shock train for the nozzle without the splitter plate, approximately $x/D_{jet} = 1.23$. The red line indicates the beginning of the oblique shock coming off the trailing edge of the splitter plate, $x/D_{jet} = 1.0$. The presence of the plate forces the initial oblique shock wave to move upstream. The splitter plate solution (Fig. 11(b)) has noticeably sharper shock and expansion waves than the non-splitter plate solution (Fig. 11(a)). This is a direct result of the techniques and priorities used when constructing the two grids. For the non-splitter plate grids, the priority was to correctly compute the discharge and thrust coefficients while reducing computational time. The grid was constructed with sufficient resolution in the streamwise direction inside the nozzle and near the exit. In the jet plume, however, the grid was rapidly stretched in the streamwise direction to reduce the number of

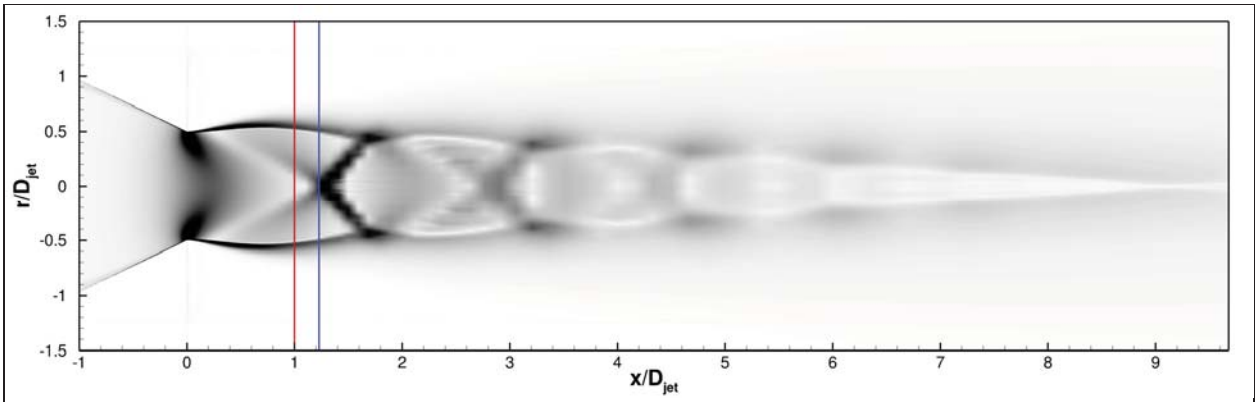

Figure 11.—Comparison of shock and expansion wave pattern for 25° conic nozzle at NPR = 4.0. Simulated Shadowgraph images (using gradient of density) are shown for Wind-US solutions. Red line indicates location of splitter plate trailing edge and induced shockwave; blue line indicates location of shock wave without splitter plate.

grid points and the computational costs. Therefore, the shock and expansion waves appear smeared in the streamwise direction for the non-splitter plate case (Fig. 11(a)). The streamwise grid spacing in the region of the oblique shock reflection is about 0.31 in. for the non-splitter plate grid. The grid for the splitter plate case was constructed with a priority to resolve the flow at the trailing edge of the splitter plate, including the shock and expansion waves for NPR = 4.0 and the vortex shedding for NPR = 1.6 (discussed more in Instance 3). The splitter plate grid has a streamwise grid spacing of about 0.14 in. in the region of the oblique shock reflection. Therefore, the shock and expansion waves for the splitter plate solution (Fig. 11(b)) appear much sharper and better defined than the non-splitter plate case. In both cases, the shock wave is spread across two to three grid cells. A much sharper shockwave would be expected if the streamwise and radial grid spacing were no larger than 0.05 to 0.1 in. in this region of the jet plume.

Figures 12 and 13 compare the Wind-US solutions and their respective experimental results for the two nozzle cases. Care was taken to align the Wind-US solutions with the experimental spark shadowgraphs, using the apparent jet exit diameter and location as the basis for scaling and alignment. However, there is still the possibility that the images may not completely align. Care was also taken to use contour coloring and levels in the Wind-US plots that best match the shadowgraph images. Due to the

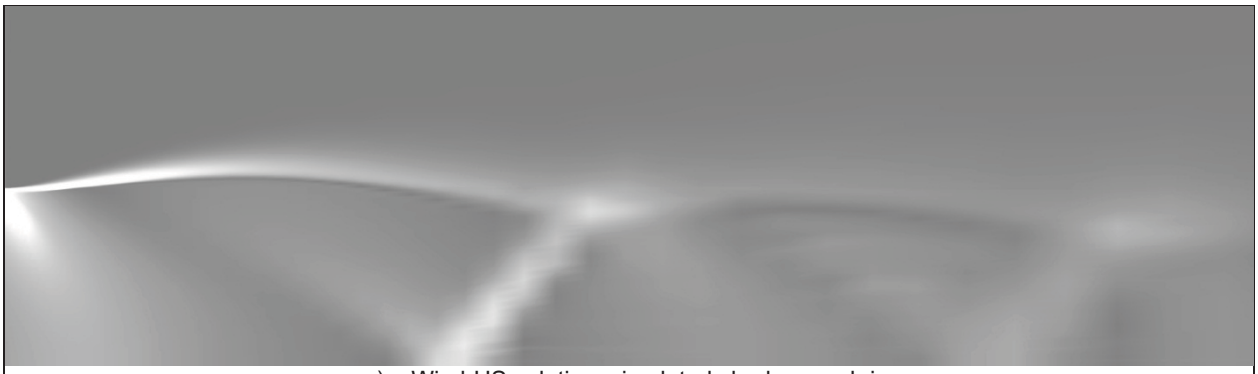

a) Wind-US solution; simulated shadowgraph image.

b) Experimental spark shadowgraph (Ref. 2).

Figure 12.—Comparison of shock and expansion wave pattern for 25° conic nozzle without splitter plate at NPR = 4.0.

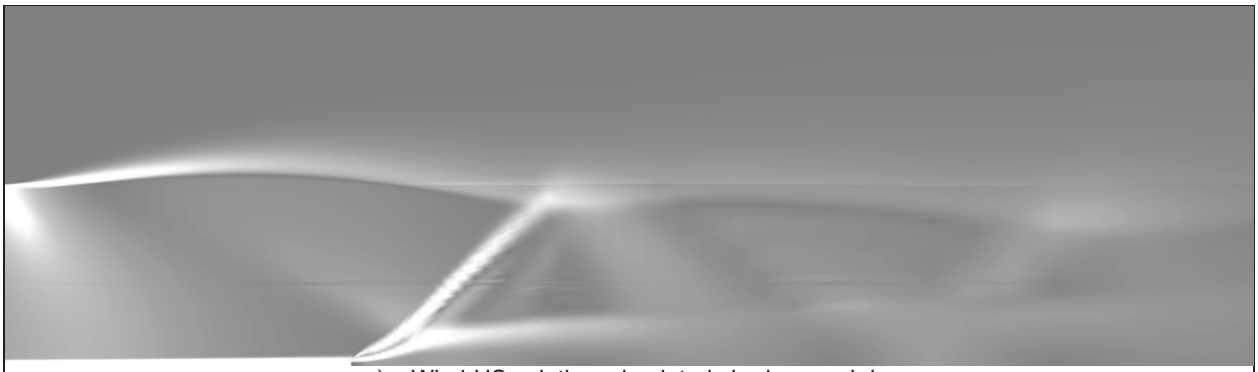

a) Wind-US solution; simulated shadowgraph image.

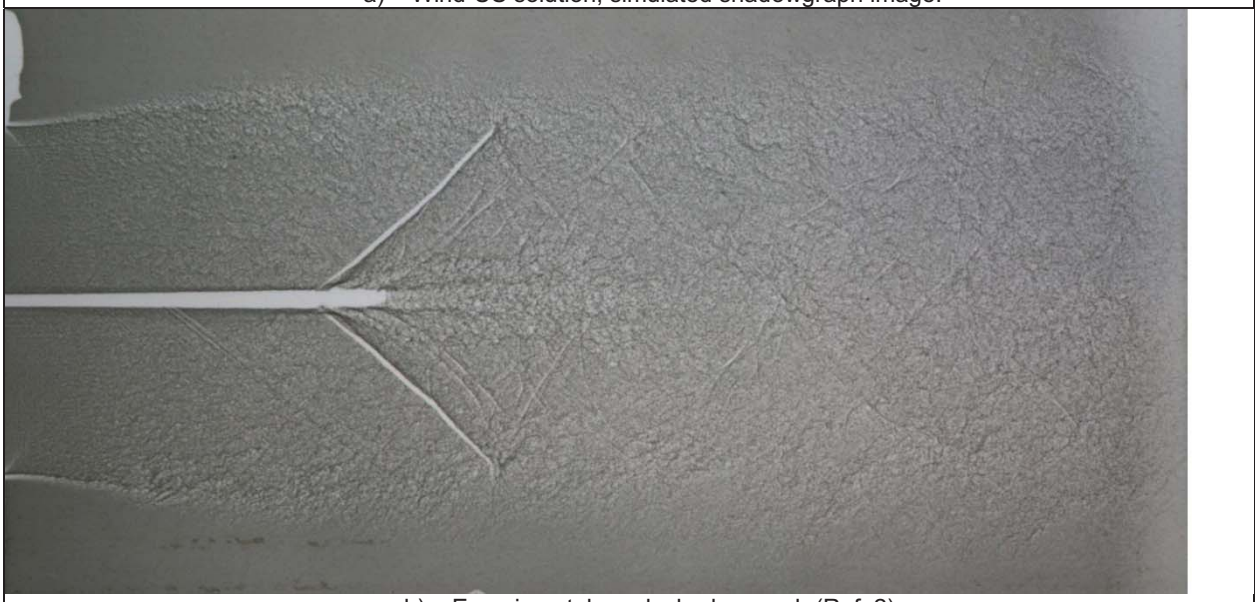

b) Experimental spark shadowgraph (Ref. 2).

Figure 13.—Comparison of shock and expansion wave pattern for 25° conic nozzle with splitter plate at NPR = 4.0.

uncertainties that exist in the comparisons of the shadowgraphs, these comparison figures (Figs. 12 and 13) should only be used to determine trends rather than absolute differences. The Wind-US solution shock locations for the non-splitter plate case show reasonable agreement with the experimental shock locations in Figure 12 for both first and second oblique shocks. As previously mentioned, the grid for this solution was constructed without adequate resolution to produce sharp shock and expansion waves in the jet plume. Therefore, it is not possible to infer more from the comparison. In Figure 13, the Wind-US solution predicts an oblique shock from the trailing edge of the splitter plate similar to what is observed in the experimental shadowgraph image. However, the Wind-US solution oblique shock appears to occur slightly further downstream than that of the experiment. Since it is difficult to discern the exact location of the splitter plate trailing edge in Figure 13(b), it is uncertain whether the Wind-US solution actually moves the oblique shock downstream or whether the discrepancy is due to a misalignment in images. While the grid of the splitter plate case shows the oblique shock much sharper than the non-splitter plate case, the shock wave is still somewhat smeared compared to the experimental photograph; the grid could be further refined to resolve the shockwave better.

Instance 3

An Unsteady Reynold-Averaged Navier-Stokes (URANS) simulation and a Detached Eddy Simulation (DES) were performed for Instance 3 for the 25° conic nozzle with splitter plate for NPR = 1.6. The goal was to produce unsteady vortex shedding that was observed experimentally. Figure 14 compares simulated shadowgraph images for the URANS solution and DES solution with the experimental shadowgraph images. The gradient of density from Equation (9) is plotted. As mentioned previously, care has been taken to scale and align the computational solutions with the experimental photograph, but uncertainty exists as the trailing edge in the experimental photograph was not discernable. The URANS and DES solutions both show vortex shedding, similar to the experimental shadowgraph, however the URANS and DES vortices appear to dissipate earlier than the experimental vortices (x/D_{jet}≈1.11 versus x/D_{jet}≈1.16). In the URANS and DES solutions, there appears to be a stronger wake downstream of the vortices, observed as streamwise streaks in the gradient of density. It is also in this wake that we see the only real difference—though small—between the URANS and DES solutions: the wake in the DES solution pinches in towards the centerline near x/D_{jet} = 1.6. The cause of the difference is unknown, but it could merely be a sign that too few time steps were run and the fluctuation in the DES solution did not have time to dissipate or convect downstream. Looking closely at the URANS and DES solutions very near the trailing edge of the splitter plate, in Figure 15, it is observed that the vortices beyond x/D_{jet} = 1.05 are only resolved by several grid points in the streamwise direction. The streamwise grid spacing is approximately 0.02 in. in this region—on the order of 30 percent of the plate trailing edge thickness. Ideally, grid spacing in this region would be on the order of 3 to 5 percent of the plate trailing edge thickness in order to resolve the vortices and not introduce numerical viscosity (Ref. 11). The lack of sufficient resolution is the probable cause of the vortices dissipating earlier than what was observed experimentally. In this case, using a grid spacing of about 2.5e-3 in. in the streamwise and radial directions through a distance of 1.25 to 1.56 in. downstream of the splitter plate (20 to 25 times the splitter plate trailing edge thickness) would ensure that the shedding, convection, and dissipation of vortices would be captured by many more grid cells.

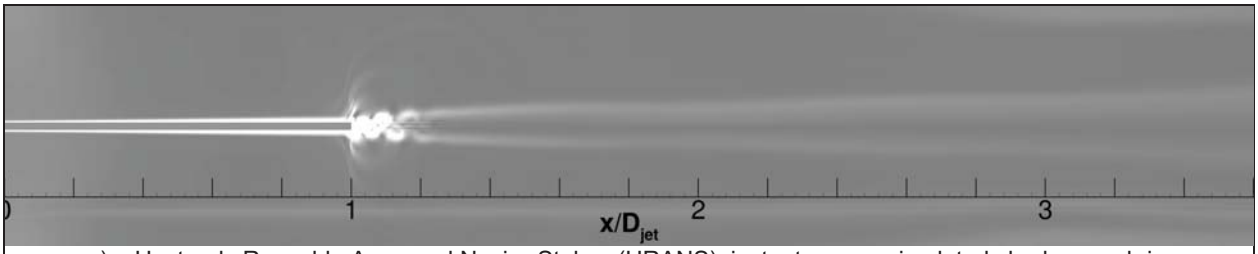

a) Unsteady Reynolds-Averaged Navier-Stokes (URANS); instantaneous simulated shadowgraph image.

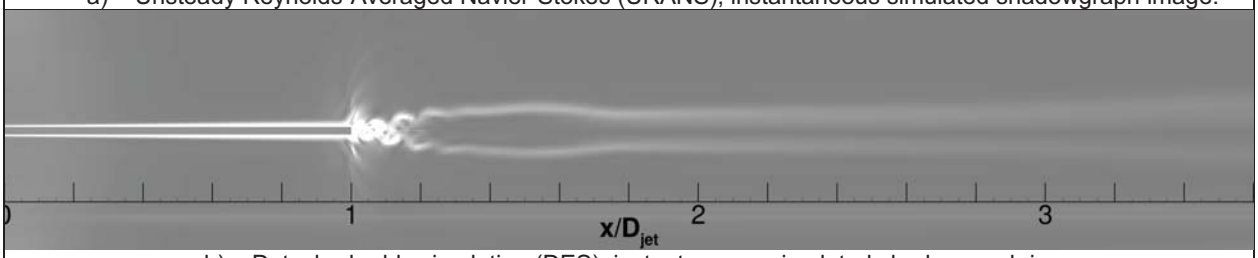

b) Detached eddy simulation (DES); instantaneous simulated shadowgraph image.

c) Experimental spark shadowgraph (Ref. 2).

Figure 14.—Vortex shedding at trailing edge of splitter plate for 25° conic nozzle with splitter plate at NPR = 1.6.

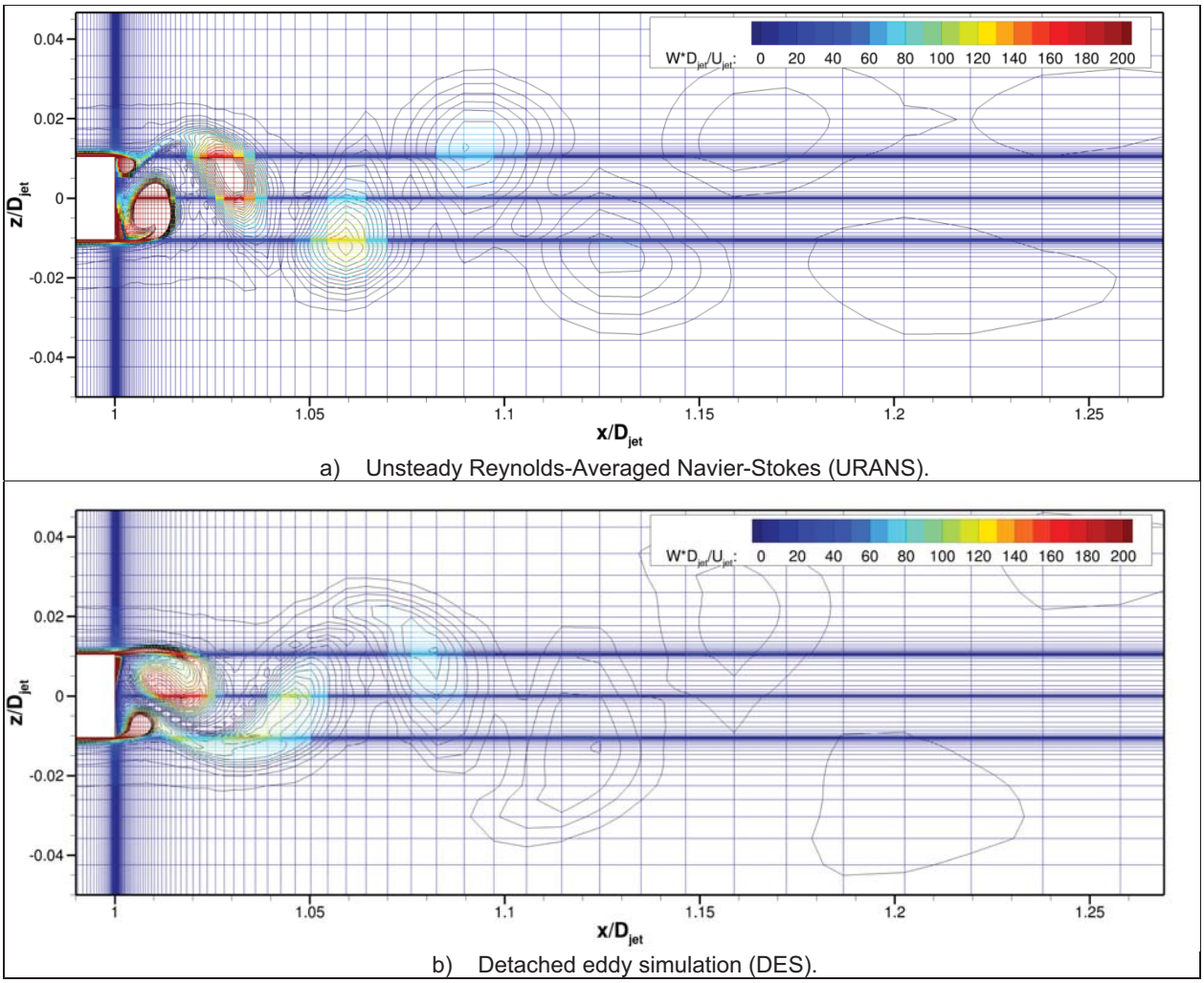

a) Unsteady Reynolds-Averaged Navier-Stokes (URANS).

b) Detached eddy simulation (DES).

Figure 15.—Detail of vortex shedding at trailing edge of splitter plate for 25° conic nozzle with splitter plate at NPR = 1.6. Grid lines shown and colored by vorticity; contour lines denote areas of equal vorticity.

Conclusions

Wind-US was used to model nozzle flows for the American Institute of Aeronautics and Astronautics (AIAA) 1st Propulsion Aerodynamics Workshop. Reynolds-Averaged Navier-Stokes (RANS) simulations were performed for 40 single-stream, axisymmetric, convergent nozzles for a range in nozzle pressure ratios (NPR) of 1.4 to 7.0. The four nozzles consisted of a circular arc reference nozzle and three conic nozzles with half angles of 15°, 25°, and 40°. The discharge coefficient, thrust coefficient, and sonic line were computed for each solution. The discharge coefficients showed excellent agreement with experimental data. The total thrust coefficient followed the general trends of the experimental data (thrust coefficients decreased as NPR increased), but were still 0.5 to 1.0 percent greater than the experimental thrust coefficients. The Wind-US sonic lines showed excellent agreement with the experimental data for NPR ≥ 2.5. For NPR = 2.0, the RANS simulations predicted the sonic lines 5 to 10 percent upstream of the experimental sonic lines.

RANS simulations were performed for the 25° conic nozzle with a splitter plate extending one diameter downstream of the exit for NPR = 4.0. The resulting patterns of shock and expansion waves were compared to a solution without the splitter plate and to experimental data. The presence of the splitter plate moved the initial oblique shockwave upstream in the flow to the trailing edge of the splitter plate. The Wind-US solution for the nozzle without the splitter plate showed reasonable agreement with

the experiment, but the lack of streamwise grid resolution in the jet plume was found to smear the shock waves. The solution with the splitter plate had sharper shock waves due to increased streamwise grid resolution in the jet plume; it showed good agreement with the experimental data. Uncertainty existed in the comparison of the experimental shadowgraph images with the RANS shadowgraph images due to difficulty in precisely aligning the location of the splitter plate trailing edges.

Unsteady Reynolds-Averaged Navier-Stokes (URANS) simulations and Detached Eddy Simulations (DES) were performed with Wind-US for the 25° conic nozzle with splitter plate for NPR = 1.6. As observed experimentally, the URANS and DES solutions produced vortex shedding from the splitter plate trailing edge. The URANS and DES vortices seemed to dissipate earlier than what was observed in the experimental shadowgraph image. A lack of grid resolution just downstream of the splitter plate trailing edge may have contributed to the numerical vortices dissipating earlier than what was observed in the experiment.

Although Wind-US successfully completed all three nozzle problem Instances of the AIAA 1st Propulsion Aerodynamics Workshop, several recommendations can be gleaned from the study. First, in order to best predict thrust, the calculations must be as representative to the experiment or hardware as possible. Future simulations must consider base regions and external surfaces in addition to simply the jet. Second, fine grid spacing [define] is necessary to properly resolve shock and expansion waves in jet plumes. Third, very fine grid resolution [define] is required to resolve unsteady phenomena—for its initial occurrence and for its propagation downstream. As propulsion systems become more complex, great care will be required to fully resolve the flow in the CFD simulations to produce better predictions.

References

1. Thornock, R.L. and Sokhey, J.S., "Propulsion Aerodynamic Workshop I, Comparison of Participant Analyses with Experimental Results for Convergent Conical Nozzle Flowfields and Performance," AIAA Paper 2013-3735, July 2013.
2. Delot, A. and Scharnhorst, R., "A Comparison of Several CFD Codes with Experimental Data in a Diffusing S-Duct," AIAA Paper 2013-3796, July 2013.
3. Winkler, C.M. and Dorgan, A.J., "BCFD Analysis for the 1st AIAA Propulsion Workshop: Nozzle Results," AIAA Paper 2013-3731, July 2013.
4. Thornock, R.L. and Brown, E.F., "An Experimental Study of Compressible Flow Through Convergent-Conical Nozzles, Including a Comparison with Theoretical Results," *Journal of Basic Engineering*, December 1972.
5. Towne, C.E., "Wind-US Users Guide, Version 2.0," NASA/TM—2009-215804, Oct. 2009.
6. Georgiadis, N.J., Yoder, D.A., Towne, C.S., Engblom, W.A., Bhagwandin, V.A., Power, G.D., Lankford, D.W., and Nelson, C.C., "Wind-US Code Physical Modeling Improvements to Complement Hypersonic Testing and Evaluation," AIAA Paper 2009-193, Jan. 2009.
7. Menter, F.R., "Two-Equation Eddy Viscosity Turbulence Models for Engineering Applications," AIAA Journal, Vol. 32, No. 8, pp. 1598-1605, Jan. 1994.
8. Georgiadis, N.J., Dudek, J.C., and Tierney, T., "Grid Resolution and Turbulent Inflow Boundary Conditions for NPARC Calculations," AIAA Paper 95-2613, July 1995.
9. Dudek, J.C., Georgiadis, N.J., and Yoder, D.A., "Calculation of Turbulent Subsonic Diffuser Flows Using the NPARC Navier-Stokes Code," AIAA Paper 96-0497, Jan. 1996.
10. NASA High-End Computing Capability Webpage, http://www.nas.nasa.gov/hecc/, March 2014.
11. Spalart, P.R., "Young-Person's Guide to Detached-Eddy Simulation Grids," NASA/CR—2001-211032, July 2001.